Optimal Aircraft Control Surface Layouts for Maneuver and Gust Load Alleviation

Bret K. Stanford*

NASA Langley Research Center, Hampton, VA, 23681

The goal of this work is to conduct aeroservoelastic optimization of a high aspect ratio transport wingbox with distributed control surfaces along the trailing edge. The control surfaces are utilized for both quasi-steady maneuver load alleviation (MLA) and unsteady gust load alleviation (GLA). The optimizer dictates the sizing details of the wingbox, the steady and unsteady control surface rotations, and also the control surface layout. Layout design variables specifically dictate which control surfaces to retain, and which to remove. The objective function is to minimize the sum of the actuator weight and the structural weight, with several imposed constraints related to structural failure and actuator saturation. The optimizer's preferences with regards to control surface layout for MLA are in strong contrast to GLA-driven designs. The GLA-driven design space also suffers from local minima not evident in the MLA space.

The results presented in this paper consider optimal control surface layouts of an aeroservoelastic wing undergoing both maneuver load alleviation (MLA) and gust load alleviation (GLA). This set of results is compared with previously-published results,[1] which considered MLA in isolation. To facilitate this exercise, a numerical model of the Common Research Model (CRM) is outfitted with 20 electro-hydraulic control surfaces spanned across the entire trailing edge, and a numerical optimizer decides which to keep, and which to remove. Those control surfaces that are removed become a rigidized facet of the outer mold line. Those that are retained can be utilized by the optimizer to actively shed aeroelastic loads: this action will alleviate the loads borne by the wingbox itself, and subsequently allow the optimizer to reduce structural weight. In order for a numerical optimizer to exploit these interdependencies, three types of design variables must be considered at once: the control surface layout, the commanded movement (static and/or dynamic) of the retained control surfaces, and the structural sizing of the wingbox. Ref. 1 considers control surface motion geared towards maneuver load alleviation (MLA) and active flutter suppression (AFS).

The current paper extends these ideas towards gust load alleviation (GLA). GLA results are obtained via state-space methods, where the aeroservoelastic equations are constructed so as to be based on a white-noise input, such that the output covariance matrix can be solved via a Lyapunov equation.[2] Methods developed in Refs. 3 - 5 are then used to accommodate stress and buckling constraints throughout the wingbox. Closed-loop control is accomplished with static output feedback (SOF),[6] where an optimal feedback matrix directly connects the available outputs (sensors) to the available inputs. This is in contrast to linear quadratic control schemes, where the controller is the same size as the plant. Methods required to accommodate SOF controllers in a gradient-based aeroservoelastic optimization process are summarized in Ref. 7.

Control surface layout is not commonly considered in aeroelastic or aeroservoelastic design.[8] This gap in the literature is not because control surface layout is an unimportant design facet, but rather due to the difficulties in handling these types of design variables (integer and/or binary) within the confines of gradient-based optimization. Examples of actuator placement via nongradient-based optimization is summarized in Ref. 9 for generic systems, and in Ref. 10 for an aeroelastic wing, but gradient-based optimization is the only feasible design tool for problems with a large number of design variables, as is often the case in integrated aeroservoelasticity.

Gradient-based optimization of control surface layouts can be accomplished by borrowing ideas from the structural continuum topology optimization literature.[11,12] In the commonly-used SIMP method (Solid Isotropic Material with Penalization), a design space is discretized into finite elements, each of which is assigned a binary design variable: solid (1) or void (0). In order to facilitate gradient-based optimization,

*Research Aerospace Engineer, Aeroelasticity Branch, bret.k.stanford@nasa.gov, AIAA Associate Fellow.

these design variables must be allowed to continuously vary between 0 and 1, but intermediate values can be implicitly penalized during the optimization process, such that the final design is composed of largely solid or void elements. The implicit penalization involves a power-law relationship between the 0-1 topology variable and the element stiffness, but a linear relationship between the topology and the element mass. This erodes the attractiveness of intermediate values (i.e., between 0 and 1) in the eyes of the optimizer, because the element stiffness obtained from a given element mass is too low.

The aeroservoelastic analogue is obtained by replacing "stiffness" with control surface through-put, via a power-law relationship between the control surface rotation commanded by the optimizer, and the value actually obtained. If the control surface topology variable is set to 1, the two values are identical; if it is 0, then actual control surface rotation is 0 as well. There is a strong conflict here that the optimizer must navigate: design variables set to 0 will allow for reductions in actuator mass, whereas variables set to 1 will allow for full movement of a given control surface, which will then shed loads off the wingbox and subsequently allow for reductions in wing structure mass, as noted above.

The remainder of this work is organized as follows: the aeroservoelastic gust equations of motion are reviewed, and the numerical methods, which allow for continuously-varying control surface topology variables, are explicitly stated. Aeroservoelastic optimization results are presented for MLA in isolation, and for simultaneous MLA and GLA. For both of those cases, results are shown for three scenarios: where the optimizer is forced to use every control surface, where the optimizer is allowed to remove as many control surfaces as it likes, and finally where the optimizer is forced to use a specified number of control surfaces. The resulting wingbox structural mass and actuator mass totals are plotted across these trends. Control surface topologies are also provided for varying limits on the allowable control surface RMS rotation rate during a gust encounter.

I. Aeroservoelastic Analysis

The linear time invariant system of the dynamic aeroservoelastic model considered here is written as:

$$\dot{\boldsymbol{x}} = \boldsymbol{A} \cdot \boldsymbol{x} + \boldsymbol{B} \cdot \boldsymbol{u} + \boldsymbol{B}_w \cdot w + \boldsymbol{F} \tag{1}$$

where $\boldsymbol{x}$ is the state vector, $\boldsymbol{u}$ is the commanded control surface rotation (as dictated by the optimizer), w is a zero-mean unit-intensity white noise, and $\boldsymbol{F}$ collects any additional forcing functions. The control surface rotations that are actually imparted onto the aeroelastic system are computed as:

$$\boldsymbol{B} = \overline{\boldsymbol{B}} \cdot \begin{bmatrix} (q_1)^p & & & \\ & (q_2)^p & & \\ & & \ddots & \\ & & & (q_N)^p \end{bmatrix} \tag{2}$$

where q_n is the topology variable for each control surface, which may vary between 0 and 1, and $\overline{\boldsymbol{B}}$ is a baseline control matrix computed with each q_n set to one. p is an integer that is typically set to 3 in the topology optimization literature.[11] The mass of the n^{th} actuator is computed as:

$$m_n = m_{0,n} \cdot q_n \tag{3}$$

where $m_{0,n}$ is the set actuator mass, and m_n is the mass actually utilized for aeroelastic analysis.

If a given q_n is set (by the optimizer) to zero, clearly the optimizer's choice for the n^{th} control surface actuation becomes immaterial, as the actuator has been removed and the control surface rigidized. If q_n is set to one, the desired control surface actuation is passed to the aeroelastic solver as-is. Intermediate values (e.g., $q_n = 0.5$) may in general be attractive to the optimizer, as they present a compromise between reducing total weight (Eq. 3) and still allowing for some contribution to maneuver load alleviation (for example) from the n^{th} control surface. Setting p to a value greater than one in Eq. 2 diminish this compromise, pushing most q_n variables to the desired extremes of zero or one during the optimization process.[11]

For static maneuver load cases, the equations reduce to:

$$\boldsymbol{A} \cdot \boldsymbol{x} + \boldsymbol{B} \cdot \boldsymbol{u} + \boldsymbol{F} = \boldsymbol{0} \tag{4}$$

where the state vector $\boldsymbol{x}$ includes the finite element solution, the aerodynamic pressures, and static trim variables. $\boldsymbol{F}$ includes jig shape loads (i.e., built-in twist of the wing), gravitational loading, and trim settings. $\boldsymbol{u}$ is a vector of quasi-steady control surface rotations, as dictated by the optimizer, and $\boldsymbol{B}$ is corrected as shown in Eq. 2. Design variables will be discussed in greater detail below, but for static MLA problems of Eq. 4, the optimizer dictates sizing design variables throughout the wingbox, the quasi-steady motion of each control surface across each load case ($\boldsymbol{u}$), and the control surface topologies ($\boldsymbol{q}$). Constraints include static stresses and panel buckling throughout the wingbox.

For dynamic gust load cases, the equations reduce to:

$$\dot{\boldsymbol{x}} = \boldsymbol{A} \cdot \boldsymbol{x} + \boldsymbol{B} \cdot \boldsymbol{u} + \boldsymbol{B}_w \cdot w \tag{5}$$

where the state vector $\boldsymbol{x}$ is now composed of modal amplitudes and velocities, lag aerodynamic states via a Rogers approximation,[13] actuator modeling terms, and gust forming filter terms. The vector $\boldsymbol{u}$ is now composed of unsteady control surface rotations. Rather than having these values explicitly dictated by the optimizer, as done in the MLA formulation above, the rotations are dictated by a closed-loop controller, and the details of that controller are imposed by the optimizer. For this work, static output feedback (SOF) is used for control. The vector of system outputs, $\boldsymbol{y}$ (sensor measurements), is given by:

$$\boldsymbol{y} = \boldsymbol{C} \cdot \boldsymbol{x} \tag{6}$$

where $\boldsymbol{C}$ is the output matrix. The goal is to find a feedback relationship of the form $\boldsymbol{u} = -\boldsymbol{K} \cdot \boldsymbol{y}$, where $\boldsymbol{K}$ is a feedback matrix, which minimizes the expected value of a performance index J:

$$J = \frac{1}{2} \cdot E\left[\int_0^\infty (\boldsymbol{x}^T \cdot \boldsymbol{Q} \cdot \boldsymbol{x} + \boldsymbol{u}^T \cdot \boldsymbol{R} \cdot \boldsymbol{u}) \cdot dt\right] \tag{7}$$

where $\boldsymbol{Q}$ is the state weighting matrix, and $\boldsymbol{R}$ is the control weighting matrix. In this work, the members of the diagonal control matrix $\boldsymbol{R}$ are utilized as optimization design variables, whereas the matrix $\boldsymbol{Q}$ is fixed across all cases.

The equations needed to compute $\boldsymbol{K}$ are reproduced from Ref. 6:

$$\boldsymbol{A}_c^T \cdot \boldsymbol{P} + \boldsymbol{P} \cdot \boldsymbol{A}_c + \boldsymbol{C}^T \cdot \boldsymbol{K}^T \cdot \boldsymbol{R} \cdot \boldsymbol{K} \cdot \boldsymbol{C} + \boldsymbol{Q} = \boldsymbol{0} \tag{8}$$

$$\boldsymbol{A}_c \cdot \boldsymbol{S} + \boldsymbol{S} \cdot \boldsymbol{A}_c^T + \boldsymbol{I} = \boldsymbol{0} \tag{9}$$

$$\boldsymbol{K} = \boldsymbol{R}^{-1} \cdot \overline{\boldsymbol{B}}^T \cdot \boldsymbol{P} \cdot \boldsymbol{S} \cdot \boldsymbol{C}^T \cdot \left(\boldsymbol{C} \cdot \boldsymbol{S} \cdot \boldsymbol{C}^T\right)^{-1} \tag{10}$$

where $\boldsymbol{A}_c = \boldsymbol{A} - \overline{\boldsymbol{B}} \cdot \boldsymbol{K} \cdot \boldsymbol{C}$, the symmetric positive semidefinite matrix $\boldsymbol{P}$ is the solution to the Ricatti equation, and $\boldsymbol{S}$ is a symmetric matrix of Lagrange multipliers. Eqs. 8-10 present a coupled set of nonlinear matrix equations for the unknowns $\boldsymbol{K}$, $\boldsymbol{P}$, and $\boldsymbol{S}$, the first two of which are Lyapunov equations.

It should be noted in the above formulation, that the uncorrected $\overline{\boldsymbol{B}}$ is used to compute the feedback matrix $\boldsymbol{K}$, but the corrected version, $\boldsymbol{B}$, is actually used for aeroservoelastic analysis in Eqs. 5 and Eqs. 6. It would be preferable to use the corrected version of $\boldsymbol{B}$ for the SOF Eqs. 8-10 as well (so that the changes in control surface topology are reflected in the computation of $\boldsymbol{K}$), but experience with the results presented below have shown that the SOF equations struggle to converge for designs with very-low q_n values, in some cases. Using $\overline{\boldsymbol{B}}$ for these iterative computations, but the corrected $\boldsymbol{B}$ for the subsequent aeroservoelastic response, is a compromise that ensures greater robustness during the optimization process.

For dynamic GLA problems of Eq. 5, the optimizer dictates sizing design variables throughout the wingbox, the members of the diagonal control matrix $\boldsymbol{R}$, and the control surface topologies ($\boldsymbol{q}$). Constraints include dynamic stresses and panel buckling throughout the wingbox, induced by the zero-mean unit-intensity white noise gust term w. These constraints are derived by first computing the state covariance matrix $\boldsymbol{X}$:

$$(\boldsymbol{A} - \boldsymbol{B} \cdot \boldsymbol{K} \cdot \boldsymbol{C}) \cdot \boldsymbol{X} + \boldsymbol{X} \cdot (\boldsymbol{A} - \boldsymbol{B} \cdot \boldsymbol{K} \cdot \boldsymbol{C})^T + \boldsymbol{B}_w \cdot U_\sigma^2 \cdot \boldsymbol{B}_w^T = \boldsymbol{0} \tag{11}$$

where U_σ is the design gust velocity.[14] Having computed the covariance matrix, methods summarized in Refs. 3 - 5 can be used to find the covariance of stress and buckling metrics throughout the wingbox, and finally failure constraint values.

II. Aeroservoelastic Sensitivities

The gradient-based optimization utilized here requires the derivatives of all of the aeroservoelastic design constraints to be computed analytically with respect to all of the design variables. This is a straightforward process for each of the equations given in the previous section, with the exception of the computation of the SOF feedback matrix $\boldsymbol{K}$. Derivatives of $\boldsymbol{K}$ are complicated by the fact that the SOF equations 8-10 are three nonlinearly-coupled matrix equations, two of which are Lyapunov equations. Ref. 7 details the computation of these sensitivities by analytically differentiating the Lyapunov equations. This process results in three new equations, which are also nonlinearly-coupled matrix equations, and must be solved once per design variable of interest.

An alternative approach to Ref. 7 is detailed here, which may be preferable in some situations. First, a residual matrix is given as:

$$\mathbb{R} = \boldsymbol{R}^{-1} \cdot \overline{\boldsymbol{B}}^{T} \cdot \boldsymbol{P} \cdot \boldsymbol{S} \cdot \boldsymbol{C}^{T} \cdot \left(\boldsymbol{C} \cdot \boldsymbol{S} \cdot \boldsymbol{C}^{T}\right)^{-1} - \boldsymbol{K} \tag{12}$$

The matrix $\mathbb{R}$, like $\boldsymbol{K}$, will have N rows and M columns, where N is the number of control surfaces and M is the number of sensors. The vectors $\mathbb{R}^*$ and $\boldsymbol{K}^*$ are flattened (vectorized) versions of these matrices. The Jacobian matrix is computed as:

$$\mathbb{J} = \partial \mathbb{R}^* / \partial \boldsymbol{K}^* \tag{13}$$

The Jacobian is a square matrix with $M \times N$ rows and columns, and is very difficult to compute analytically. It can, however, be computed via a complex step perturbation.[16]

First, the n^{th} member of $\boldsymbol{K}^*$ is perturbed by a small complex number: $\boldsymbol{K}^*_n \rightarrow \boldsymbol{K}^*_n + i \cdot \delta$. Using this complex $\boldsymbol{K}^*$, complex matrices $\boldsymbol{P}$ and $\boldsymbol{S}$ are found from Eqs. 8 and 9 (methods required for a Lyapunov solution with complex numbers are detailed in the Appendix), and a complex residual is found from Eq. 12. The n^{th} column of $\mathbb{J}$ is then

$$\mathbb{J}_n = imag(\mathbb{R}^*)/\delta \tag{14}$$

This perturbation process must be repeated for all $M \times N$ members of $\boldsymbol{K}^*$, resulting in a fully-assembled Jacobian. If desired, a recursive Newton iteration scheme can be used, via the residual and the Jacobian, to compute the optimal SOF feedback matrix $\boldsymbol{K}$, as opposed to the original equations Eqs. 8-10. The main utility of these terms, however, is that they can be used to compute derivatives of $\boldsymbol{K}$ via an adjoint method.[17]

For a given design variable, s, each of the design-dependent aeroservoelastic matrices ($\boldsymbol{A}$, $\boldsymbol{B}$, $\boldsymbol{C}$, $\boldsymbol{R}$) are perturbed with a small complex step. For example:

$$\boldsymbol{A} \rightarrow \boldsymbol{A} + i \cdot \delta \cdot (\partial \boldsymbol{A} / \partial s) \tag{15}$$

where the derivatives of $\boldsymbol{A}$, $\boldsymbol{B}$, $\boldsymbol{C}$, and $\boldsymbol{R}$ with respect to s are easily computed in an analytical manner, and s represents any of the design variables discussed above. Having perturbed each of these matrices via Eq. 15, complex matrices $\boldsymbol{P}$ and $\boldsymbol{S}$ are again found from Eqs. 8 and 9, and a complex residual found from Eq. 12. The final sought-after derivative is computed via an adjoint solve:

$$\partial \boldsymbol{K}^* / \partial s = \mathbb{J}^{-1} \cdot (-imag(\mathbb{R}^*)/\delta) \tag{16}$$

This is a process that must be repeated for each design variable of interest.

III. Optimization Test Case

The demonstration case considered here is a metallic wingbox of the Common Research Model,[15] a generic swept-wing subsonic transport configuration with an aspect ratio of 13.5 shown in Fig. 1. The optimization desires to identify the configuration with the lowest mass, which can still withstand the static maneuver loads and gust loads (both with and without the assistance of twenty trailing edge control surfaces distributed from root to tip, also seen in Fig. 1) and also remain flutter-free. The objective function is specifically the sum of the wingbox structural mass and the distributed actuator mass. Detailed information regarding this optimization problem can be found in Refs. 1 and 5; only cursory details are provided here. Four types of design variables are considered by the gradient-based optimizer:

1. Structural sizing: the skin panels, ribs, and spar sections of the wingbox are discretized into design patches with smeared stiffeners. The shell thickness, stiffener thickness, and stiffener height is optimized separately for each design patch.
2. Maneuver load alleviation: the optimizer dictates the static deflection of each control surface across two closed-loop static aeroelastic maneuver loads ($-1g$ and $2.5g$). Two additional open-loop maneuver loads are applied without the use of MLA as well, which the optimizer must satisfy passively using the sizing variables alone.
3. Gust load alleviation: the members of the diagonal control weighting matrix $\boldsymbol{R}$ are utilized as design variables as well (one per control surface). The output matrix $\boldsymbol{C}$ is based on six accelerometers distributed throughout the wing. This control architecture in turn dictates the closed-loop gust response. As with the static maneuver loads, an open-loop gust load is applied as well, which the optimizer must satisfy passively using the sizing variables alone.
4. Control surface topology: the optimizer sets the vector $\boldsymbol{q}$, which dictates the control through-put (Eq. 2) and actuator mass (Eq. 3).

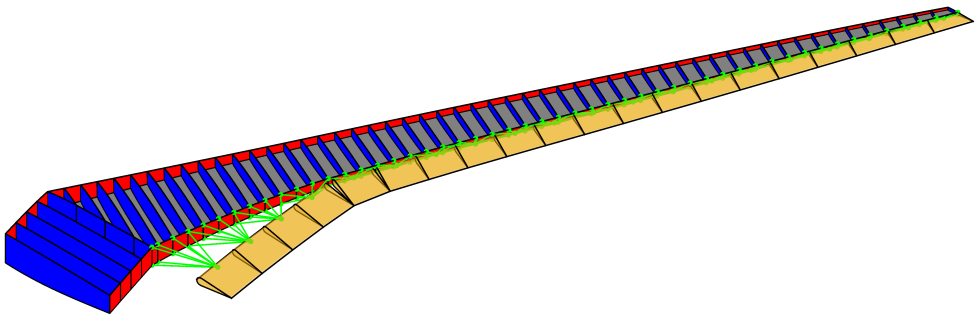

Figure 1. Wingbox and control surfaces of the high aspect ratio CRM.

Several categories of design constraints must be satisfied during the optimization process:

1. Static stresses: during each maneuver load (both open-loop, and closed-loop via MLA), the stresses of each wingbox finite element must be within the failure envelope.
2. Static buckling: during each maneuver load, the buckling factor of each stiffened panel must be within the failure envelope.
3. Flutter: the airplane must be free of instability up to 15% of the dive speed (i.e., the eigenvalues of $\boldsymbol{A}$ must be in the left-half-plane).
4. Dynamic stresses: during the continuous gust load (both open-loop, and closed-loop via GLA), the equal-probability stress hypersurface[4] of each wingbox finite element must be within the failure envelope.
5. Dynamic buckling: during the continuous gust load, the equal-probability buckling hypersurface of each stiffened panel must be within the failure envelope.
6. Control surface RMS (root mean square) rate: during the closed-loop continuous gust, the RMS rate of each control surface must be less than a prescribed acceptable rate limit.

Constraint-aggregation[18] is used to reduce the number of constraints to an acceptable level, for each of these categories.

For this work, various design variables and constraints are phased in gradually, in order to better understand their individual impact on the mass-reduction optimization process, and the synergies between them.

IV. Results

The first set of results shown here, Fig. 2, only include static aeroelastic physics with MLA, and is reproduced from Ref. 1. Two maneuver loads are presented. For each load case, the quasi-steady control surface rotations are shown for when the optimizer is forced to use all 20 control surfaces (i.e., each member of the topology vector $\boldsymbol{q}$ is fixed at 1), and when the optimizer is allowed to remove some control surfaces.

For the former case, during the 2.5g maneuver, the optimizer utilizes positive in-board rotations (positive lift generation) to maintain trim, negative rotations further out-board (to alleviate loads on the flexible wing), and relatively-small rotations at the wing tip. Small tip rotations are driven by the large aspect ratio of this highly-flexible wing: these control surfaces have low effectiveness, as their pitching moment is typically counteracted by excessive torsional rotation.

When the control topology variables are activated, the optimizer removes all but 7 control surfaces: the two closest the root, two near span station 20 m, and three near span station 30 m. These seven control surface rotations all approach the design variable bounds of ± 10 deg., whereas the previous case where all surfaces were active, did not approach these bounds. In activating the control surface topology variables, the actuator mass drops from 2,262 kg to 812 kg. The structural wingbox mass increases, slightly, from 13,862 kg to 14,043. This increase is due to the fact that there are fewer control surfaces, weakening the ability of the optimizer to apply MLA, and thereby forcing the optimizer to stiffen the wingbox and bear those loads passively. The objective function, the sum of structural and actuator weight, decreases from 16,124 kg to 14,852 kg. The mild penalty paid by dropping from 20 to 7 control surfaces, in terms of the total mass, indicates that MLA with all 20 surfaces is only slightly more effective than using just 7.

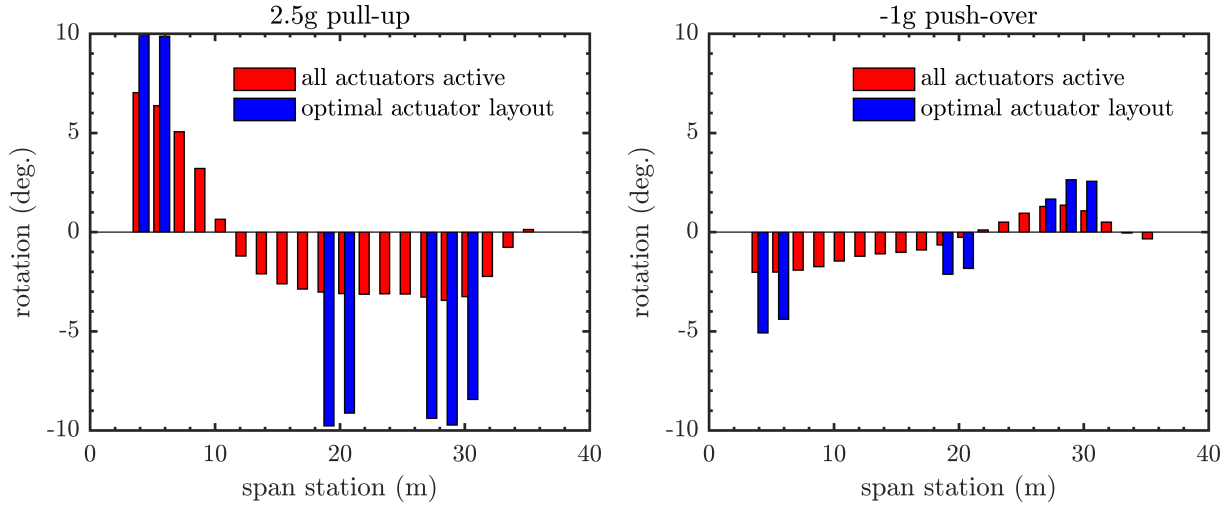

Figure 2. Optimal control surface rotation design variables during MLA.

Next, Fig. 3 shows results when the optimizer is forced to use less than 7 control surfaces, via the introduction of a constraint on the total number of control surfaces. This constraint is progressively lowered from 7 to 0, and a complete optimization is run for each setting. The left side of the figure shows the change in structural and actuator mass as this constraint is lowered; the right side shows the change in the control surface topology. The objective function (sum of structural and actuator mass) is relatively unchanged between 3 and 7 control surfaces, as the structural mass penalty is largely offset by the drop in actuator mass. When forced to use just 3 control surfaces, the optimizer chooses the two at the root, and one near mid-span.

Below 3 control surfaces in Fig. 3, the basic balance between in-board lift generation (for trim) and out-board load alleviation is destroyed, and the structural mass penalty is large. The last control surfaces that the optimizer is willing to give up are at the root, which indicates the important role that trim plays in MLA. Root rotations implicitly alleviate loads into the wingbox by allowing the airplane to fly at a lower angle of attack. Lower aspect ratio wings may see greater benefit to having a single control surface out-board, which can explicitly alleviate loads: for the high aspect ratio seen here, however, these out-board surfaces possess degraded effectiveness. The final structural mass in Fig. 3, when all of the control surfaces have been removed, is 19,835 kg. In this extreme case, all of the maneuver loads are borne passively by the wingbox, which must therefore by very stiff/heavy.

The previous results have been reproduced from Ref. 1 in order to place the remainder of this paper in context. Specifically, this process is repeated with the inclusion of dynamic aeroelastic effects, as summarized above. The control surfaces are now tasked with both MLA and GLA (conceptually, these will not occur simultaneously, as MLA is implemented during maneuvers, and GLA during cruise), and in choosing the

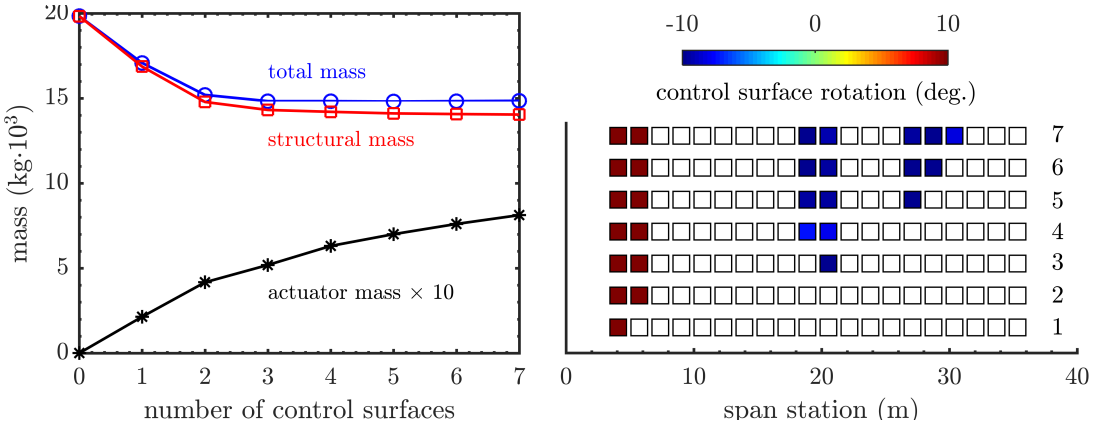

Figure 3. Shift in optimal mass properties (left) and optimal control surface layout (right), with changes in the required number of control surfaces, for MLA.

optimal control surface layout, the optimizer must compromise between the two. Results are shown in Fig. 4, for a closed-loop control surface RMS rate limit, during the gust encounter, of 50 deg./s (the results during MLA, which is being optimized concurrently, are not shown here, as they are conceptually similar to the results shown in Figs. 2 and 3). Typically, actuator saturation is assumed to be unlikely if the rate saturation value is at least 3 standard deviations (i.e., RMS values). Each actuator along the trailing edge is a different size, and will have a different rate limit: the same RMS limit is imposed on each actuator for this work, however, for simplicity.

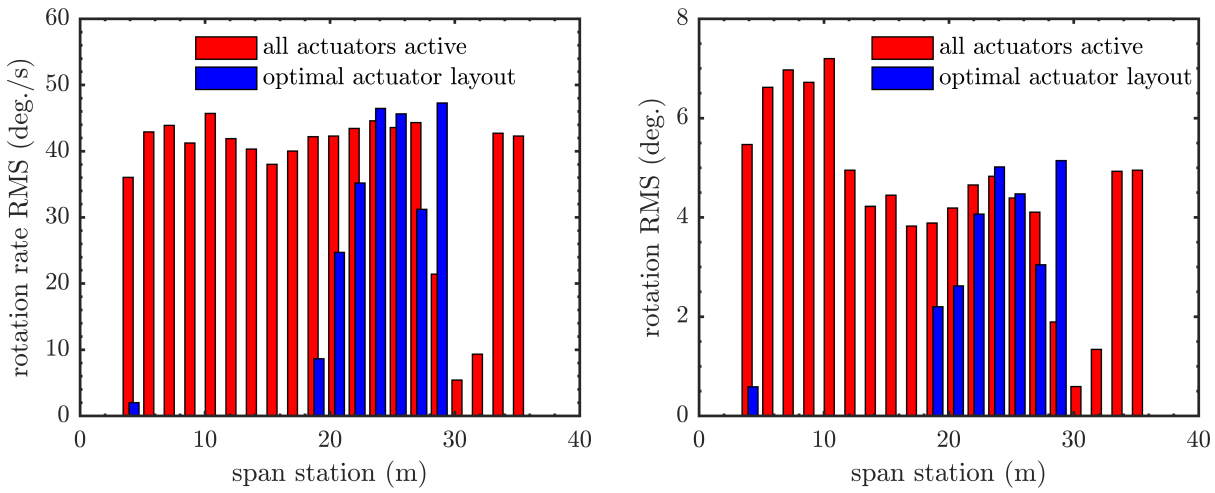

Figure 4. Optimal control surface rotation RMS response during GLA of the resulting optimal control surface layout when simultaneously considering MLA and GLA.

Fig. 4 shows the RMS rotation rate for the situation when the optimizer is forced to use all 20 control surfaces (i.e., each member of the topology vector $\boldsymbol{q}$ is fixed at 1), and the optimal RMS rates obtained when the optimizer is allowed to remove some control surfaces. The right side of the figure shows the rotation RMS values (rather than the rates). These values are not utilized by the optimizer, but plotting them here provides a more comprehensive view of the spatial control power distribution utilized by the optimizer. For the situation where the optimizer uses all 20 control surfaces, most of the RMS rates are near the imposed limit of 50 deg./s. None of the rates are actually at the limit, owing to the conservatism of the constraint-aggregation[18] method used. Rotation RMS values are on average 5 deg. (with higher values at the root): if all the control power was focused on a single frequency, that frequency would be roughly 1.6 Hz. For the continuous gusts considered here, of course, no single frequency is dominant in actuality.

When the control topology variables are activated, the optimizer removes all but 8 control surfaces: one

at the root, and then 7 adjacent surfaces between span stations 20 and 30 m. Unlike the case when all surfaces are active, here only 3 of the 8 retained surfaces approach the rate limit of 50 deg./s. This is likely due to the fact that the optimizer is forced to provide a compromise between MLA and GLA. This is particularly true for the control surface at the root, which has been shown previously to be extremely important for MLA, but of little utility for GLA as evidenced by its low RMS values.

Figure 5 repeats the exercise of Fig. 3 with unsteady aeroelasticity now included. Now, the constraint on the allowable number of control surfaces is progressively lowered from 8 (the value that the optimizer chooses naturally) to 0, with a complete optimization run for each setting. There are several interesting differences between this figure and Fig. 3. First, it can be seen that the root control is the very first control surface that the optimizer removes, when forced to drop from 8 to 7 surfaces. This is in strong contrast with Fig. 3, where the root surface is the very last surface that the optimizer removes. This discrepancy would imply that the compromise between MLA and GLA in Fig. 4 favors GLA.

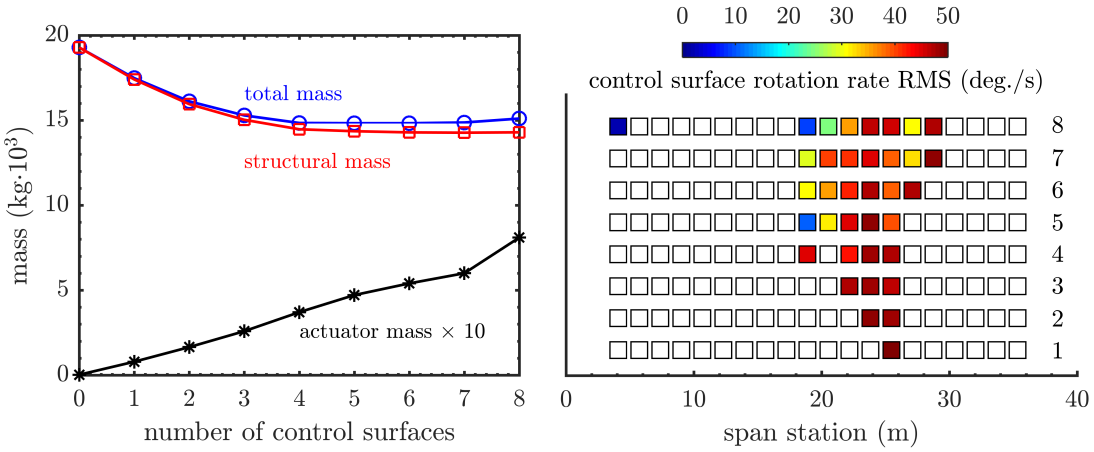

Figure 5. Shift in optimal mass properties (left) and optimal control surface layout (right), with changes in the required number of control surfaces, for simultaneous MLA and GLA.

Secondly, the total mass (structural mass plus the total actuator mass) on the left side of the figure, when dropping from 8 to 7 control surfaces, decreases. As this is the objective function of the optimization problem, this decrease would imply that the 8-surface result is a local minimum. No control surface limit had been applied during the 8-surface result, and so in an effort to minimize the objective, the optimizer should have been able to find the 7-surface design, which is lighter. Instead, the optimizer gets "stuck" in the local minimum of the 8-surface design. In fact, continually dropping the number of control surfaces below 7 sees the objective function continue to decrease (only slightly, and not visually evident in Fig. 5) all the way down to 5 surfaces. Only when the optimizer shifts from 5 to 4 surfaces, does the objective function finally increase (degrade). This, again, is in strong contrast with Fig. 3, where every leftward shift on the plot sees a degradation in the objective. The true minimum of Fig. 5 is then the case with 5 control surfaces, which has no retained control surfaces at the root at all, a further indication that GLA is a stronger design driver than MLA here.

Substantial degradation of the objective function occurs when the optimizer drops below 3 control surfaces, and the final control surface retained is near span station 25 m. As the number of control surfaces decreases, the RMS rates of the retained surfaces converge closer to the rate limit of 50 deg./s. This is largely due to the fact that the conservatism of the constraint aggregation weakens, with fewer constraints included in the aggregation process.

Finally, the relationship between the rate limit constraint boundary and the subsequent optimal control surface layout, is explored in Fig. 6. Values of 50 (repeated from above), 30, and 20 deg./s are utilized. The optimal layouts for the two lower values do not retain the root surface, an indication that GLA prioritization over MLA continues to increase when the GLA-centric constraints (i.e., RMS rate limit) are made harder to satisfy. The 30 deg./s design retains 8 adjacent control surfaces between stations 20 and 30 m., while the 20 deg./s design further removes the 4th control surface in that set. The rotation RMS values on the right side of this figure (again not used by the optimizer, but only shown here for illustrative purposes) shows a control surface for the 20 and 30 deg./s constraints with relatively large rotation amplitudes. For the 20

deg./s case, the rotation RMS approaches 10 deg. Again assuming that all control power is focused on a single frequency (which is not the case), this would result in a low frequency of roughly 0.3 Hz. The design driver behind such a result is unclear, but may be due to rigid body modes, which are important for this high aspect ratio configuration.[5]

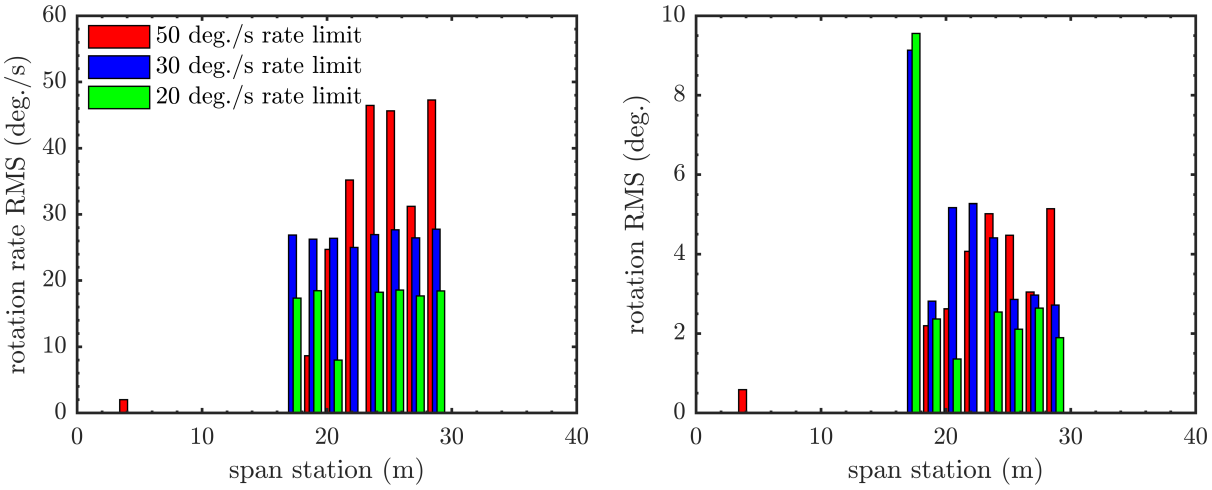

Figure 6. Optimal control surface rotation RMS response during GLA, for different RMS rate limits.

V. Conclusions

This paper has considered the optimal control surface layouts of an aeroservoelastic wing undergoing both maneuver load alleviation (MLA) and gust load alleviation (GLA). The results here are compared with previously-published results[1] that considered MLA in isolation. Several conclusions about this aeroservoelastic design space can be made: first, the design space is very flat, in the sense that numerous control surface layouts provide very similar objective functions (the sum of the actuator weight and the structural weight). Reductions in the number of control surfaces drops the actuator weight, but is typically offset by increases in structural weight (as the optimizer must shift from active load alleviation to passive load alleviation owing to the reduced number of control surfaces), leaving the total objective function minimally changed. Only when the optimizer is forced to use very-few actuators (typically 3 or 4), does the structural weight penalty finally outweigh the actuator weight drop, and the total objective function suffers.

Secondly, the above observation is found for both MLA and GLA designs, though the layouts favored by the two alleviation schemes are substantially different, with MLA-driven designs biased towards in-board control surfaces (for trim-related reasons), and GLA-driven designs biased towards control surfaces further out-board along the span. Neither configuration utilizes control surfaces at the wing tip of the high aspect ratio wing, as those mechanisms have very-low effectiveness, and are even reversed for some flight conditions.

Finally, it is noted that the GLA-driven designs suffer from convergence towards local minima, an issue not explicitly noted on the MLA-driven designs (though the design space here is large enough that it is impossible to clarify if a given design is global in nature). When the optimizer is forced to use fewer control surfaces than its natural preference (for GLA, this number is 8), the objective function actually decreases until the number of control surfaces reaches 5. If not for the multi-modality of the design space, the optimizer should have found this 5-surface design on its own, in an effort to minimize the objective. For MLA, on the other hand, the optimizer naturally converges to a 7-surface design: forcing the optimizer to use less results in a degradation of the objective. This GLA-centric multi-modality is perhaps not surprising, given the substantial complexities involved in optimizing the feedback matrix, $\boldsymbol{K}$, for unsteady closed-loop simulations.

References

[1]Stanford, B., "Optimal Control Surface Layout for an Aeroservoelastic Wingbox," *AIAA Journal*, Vol. 55, No. 12, pp. 4347-4356, 2017.

[2]Zole, A., Karpel, M., "Continuous Gust Response and Sensitivity Derivatives Using State-Space Models," *Journal of Aircraft*, Vol. 31, No. 5, pp. 1212-1214, 1994.

[3]Engelsen, F., Livne, E., "Quadratic Stress Failure Constraints for Structures under Combined Steady and Random Excitation," *AIAA Journal*, Vol. 42, No. 1, pp. 132-140, 2004.

[4]Engelsen, F., Livne, E., "Modal Acceleration Based Random Gust Stresses in Aeroservoelastic Optimization," *Journal of Aircraft*, Vol. 41, No. 2, pp. 335-347, 2004.

[5]Stanford, B., 'Aeroservoelastic Optimization of a Transport Aircraft Wingbox under Stochastic Gust Constraints," *Journal of Aeroelasticity and Structural Dynamics*, Vol. 6, No. 1, pp. 21-41, 2018.

[6]Stevens, B., Lewis, F., *Aircraft Control and Simulation*, John Wiley and Sons, Hoboken, NJ, 2003.

[7]Stanford, B., 'Gradient-Based Aeroservoelastic Optimization with Static Output Feedback," *Journal of Guidance Control and Dynamics*, Vol. 42, No. 10, pp. 2314-2318, 2019.

[8]Livne, E., "Integrated Aeroservoelastic Optimization: Status and Direction," *Journal of Aircraft*, Vol. 36, No. 1, pp. 122-145, 1999.

[9]Padula, S., Kinkaid, R., "Optimization Strategies for Sensor and Actuator Placement," NASA/TM-1999-209126.

[10]Kolonay, R., Kobayashi, M., "Optimization of Aircraft Lifting Surfaces using a Cellular Division Method," *Journal of Aircraft*, Vol. 52, No. 6, pp. 2051-2063, 2015.

[11]Bendsøe, M., Sigmund, O., *Topology Optimization - Theory, Methods, and Applications*, Springer, New York, 2003.

[12]Deaton, J., Grandhi, R., "A Survey of Structural and Multidisciplinary Continuum Topology Optimization: Post 2000," *Structural and Multidisciplinary Optimization*, Vol. 49, pp. 1-38, 2014.

[13]Roger, K., "Airplane Math Modeling Methods for Active Control Design," AGARD CP-228, pp. 4-11, 1977.

[14]Hoblit, F., *Gust Loads on Aircraft: Concepts and Applications*, AIAA, Washington DC, 1988.

[15]https://commonresearchmodel.larc.nasa.gov, retrieved October 2018

[16]Martins, J., Sturdza, P., Alonso, J., "The Complex-Step Derivative Approximation," *ACM Transactions on Mathematical Software*, Vol. 29, pp. 245-262, 2003.

[17]Adelman, H., Haftka, R., "Sensitivity Analysis of Discrete Structural Systems," *AIAA Journal*, Vol. 24, No. 5, pp. 823-832, 1986.

[18]Kreisselmeier, G., Steinhauser, R., "Systematic Control Design by Optimizing a Vector Performance Index", *International Federation of Active Controls Symposium on Computer-Aided Design of Control Systems*, Zurich, Switzerland, 1979.

Appendix: Complex Lyapunov Solvers

The Lyapunov solvers required in Eqs. 8 and 9 are not "complex step-safe", in that complex inputs into these codes produce only real-valued outputs. Some modification to these solvers is therefore required for complex step derivatives. A generic Lyapunov equation is written as:

$$\boldsymbol{A} \cdot \boldsymbol{X} + \boldsymbol{X} \cdot \boldsymbol{A}^T + \boldsymbol{Q} = \boldsymbol{0} \tag{17}$$

Each of these terms can be broken into a large real part and a small imaginary part:

$$(\boldsymbol{A}_r + i \cdot \delta \cdot \boldsymbol{A}_i) \cdot (\boldsymbol{X}_r + i \cdot \delta \cdot \boldsymbol{X}_i) + (\boldsymbol{X}_r + i \cdot \delta \cdot \boldsymbol{X}_i) \cdot (\boldsymbol{A}_r + i \cdot \delta \cdot \boldsymbol{A}_i)^T + (\boldsymbol{Q}_r + i \cdot \delta \cdot \boldsymbol{Q}_i) = \boldsymbol{0} \tag{18}$$

If one expands these products, and ignores any terms proportional to δ^2, then $\boldsymbol{X}_r$ can be computed via a Lyapunov solve from the real terms in the expansion:

$$\boldsymbol{A}_r \cdot \boldsymbol{X}_r + \boldsymbol{X}_r \cdot \boldsymbol{A}_r^T + \boldsymbol{Q}_r = \boldsymbol{0} \tag{19}$$

The imaginary part is finally computed with a second Lyapunov solve:

$$\boldsymbol{A}_r \cdot \boldsymbol{X}_i + \boldsymbol{X}_i \cdot \boldsymbol{A}_r^T + \boldsymbol{A}_i \cdot \boldsymbol{X}_r + \boldsymbol{X}_r \cdot \boldsymbol{A}_i^T + \boldsymbol{Q}_i = \boldsymbol{0} \tag{20}$$